

6 *Active Surface Wave Phase Velocity Estimation*

A mathematical problem should be difficult in order to entice us, yet not completely inaccessible, lest it mock at our efforts.

David Hilbert, *International Congress of Mathematicians Speech*, Paris, 1900

6.1 Introduction

Advanced spatial array and digital signal processing methods yield significant improvements in the analysis of active seismic surface wavefields. To unambiguously determine wavenumber, either direction of propagation or wave velocity must be known. In active surface wave problems, since the location of the source is known, analysis of active surface wave tests simplifies to a scalar problem. Therefore, only a single scalar wavenumber, k_x , must be estimated from a linear array of receivers. With a few assumptions about the statistical properties of the background seismic noise field, measurements from a traditional SASW test setup, i.e. only two sensors with a varying separation distance, can be combined to yield single mode and multiple mode phase velocity estimates with synthetic linear arrays. Compared to the traditional two-point estimators, advanced DSP methods can sift out multiple modes of propagation and reduce the error due to the near-field model incompatibility. Cylindrical spatial array estimators offer the ability to introduce the correct physical model and improve phase velocity estimates. Although cylindrical estimators offer better wavenumber estimates, the plane wave estimators offer considerable computational savings through implementation of the Fast Fourier Transform, as outlined in Appendix A.

The dispersion relation for the ISC '98 site will be determined using the advanced signal processing methods discussed in Chapter 4. After displaying the results of applying the plane wave estimation methods, a cylindrical model estimator will be introduced, and

the difference between the plane and cylindrical wavefield models will be discussed. In subsequent sections, multiple modes of propagation will be isolated and an alternative phase velocity estimation method will be considered.

6.2 Previous Studies and Recommendations

Several analytical and numerical studies have been conducted to determine the magnitude of near-field and body wave interference effects on estimated dispersion curves from experimental measurements (Tokimatsu, 1995; Sanchez-Salinero, 1987). Despite analyzing the problem with different procedures, the studies yield similar conclusions regarding the most important limitations of the traditional seismic surface wave analysis procedures. Despite the recognition of similar problems, the recommendations to mitigate the perceived problems vary considerably.

Tokimatsu and Tamura (1995) explicitly divided the displacements of the seismic wavefield into the components due to Rayleigh surface waves and body waves. Then, for different profiles, the magnitude of dimensionless displacements due to Rayleigh and body waves, as a function of dimensionless distance, were calculated. The study concluded that the body waves could not be neglected, especially for inversely dispersive profiles, for distances of up to two wavelengths or greater from the source.

In another numerical study, Sanchez-Salinero (1987) created synthetic dispersion curves based on finite element models for a homogeneous half-space and various layered profiles. Two sensors were placed at various positions, where d_1 = the distance between the source and first receiver, and d_2 = the distance between the first and second receivers. The homogeneous half-space dispersion curve yielded good results when $d_1 > 2\lambda$, but the phase velocity estimations for lower frequencies were lower than expected. The incorrect velocity estimates have been attributed to near-field effects, i.e. coupling of body and Rayleigh waves near the source (Sanchez-Salinero, 1987).

The two studies completely characterize the major problems of traditional estimators, which are discussed in the next section. The inability to handle multiple modes leads to the perceived body wave interference effects at distances larger than two wavelengths from the source, and the model incompatibility leads to the lower than expected phase velocity estimates at lower frequencies.

6.3 The Categories of Traditional Surface Wave Analysis Limitations

Previous numerical and experimental studies vividly display the limitations of traditional engineering analysis of actively produced seismic surface waves. The limitations of traditional surface wave phase velocity estimators can be placed into three categories, which were briefly mentioned in Chapter 1.

The three categories will be introduced, their most important characteristics discussed, and the path for the removal of their detrimental effects outlined. Much of the traditional estimator limitations simply stem from using a two-point estimator. Although concepts such as resolution and spectral characteristics really do not apply to the two-point estimator, in a general sense, the two-point estimator has very poor resolution, sidelobe, and noise control characteristics.

6.3.1 Model Incompatibility Effect

The model incompatibility of estimating parameters with a plane wave model, while the experimentally measured wavefield follows cylindrical propagation, has muddled the estimation of both phase velocity and attenuation. The model incompatibility has even influenced theoretical and numerical studies, where complete and physically correct Green's functions have been used to create synthetic data. The recommendations from several theoretical studies depend on estimating plane wave model parameters from the physically correct Green's function.

Section 6.10 discusses the effects of the model incompatibility completely, since the problem offers a straight-forward analysis. The synthetic linear array plane wave conventional and adaptive spectrum estimators yield much better phase velocity estimates than the traditional two-point methods, but the optimum solution comes from the cylindrical power spectrum estimation problem. Section 6.11 derives and discusses optimum cylindrical beamformers.

6.3.2 Near-field Body Wave Interference

The near-field body wave interference problem refers to the reflected body wave energy at the interface between two soil layers and near the source. Part, or possibly all, the reflected body wave energy contributes to additional Rayleigh wave modes. The complexity of the near-source wavefield, although the ray paths and superposition effects can be modeled, has led to the common use of "near-field" effects to explain away unexpected experimental results. As Section 6.10 shows, the model incompatibility influences the traditional near-field effects to a greater extent than possible near-field body wave interference.

Although a complete study of the superposition effects is required to determine the amount of body wave energy reflections that contribute to additional Rayleigh surface wave modes, several important concepts should be recognized, including the following:

- 1.) The type and amount of energy reflected at the boundary between two soil layers depends on the contrast in elastic parameters, mass density, and the angle of incidence,
- 2.) Once the body wave energy reflects and contributes to an additional Rayleigh surface wave mode, the energy begins propagating cylindrically and tends to a decay rate of \sqrt{x} ,
- 3.) Spherically spreading body waves propagating along the surface of the earth are still subject to partial orthogonality with the Rayleigh surface wave wavenumbers, creating a natural decrease in their negative impacts.

The near-field body wave effects will be revisited when discussing active surface wave material attenuation coefficient estimation in Chapter 7.

6.3.3 Far-field Body Wave Interference

The desire to limit the near-field effects in traditional surface wave estimators has out-weighed the desire to isolate multiple modes. Reflecting and superposing body wave energy contributes to multiple mode surface wave propagation, which allows more information to be extracted from the propagating wavefield if the multiple modes can be isolated.

When analyzing traditional estimators, the near-field criteria has been extended in inversely dispersive profiles due to unexplained results, extending the near-field out to greater than two wavelengths. The problem actually stems from the presence of multiple modes, which result from far-field superposition of body waves. The inability of traditional estimators to handle multiple modes has led to the more restrictive near-field requirements, but the recourse once again to the near-field explanation, even in a case when a near-field in any common meaning of the word plays no role in the problem, serves to expose the dead hand of the near-field on geotechnical surface wave analysis. The problem of multiple modes, or far-field superposition of body waves, is completely handled by the synthetic linear array conventional and adaptive frequency-wavenumber power spectrum estimators.

6.3.4 Summary

An overview of the final conclusions regarding the limitations of traditional seismic surface wave analysis includes the following:

- 1.) The effects due to body wave interference have been over-estimated,
- 2.) The effects due to the inapplicability of the far-field assumption can easily be determined and are discussed in Section 6.10,
- 3.) The two traditionally lumped problems, i.e. the *model incompatibility effects* and the *near-field body wave effects*, should be considered separately.

Although the separation recommended in 3.) may seem trivial and almost obvious, the lumping of these two effects together into the traditional geotechnical near-field effects has been the source of muddled recommendations and experimental conclusions.

6.4 Rayleigh Surface Waves from Active Point Sources

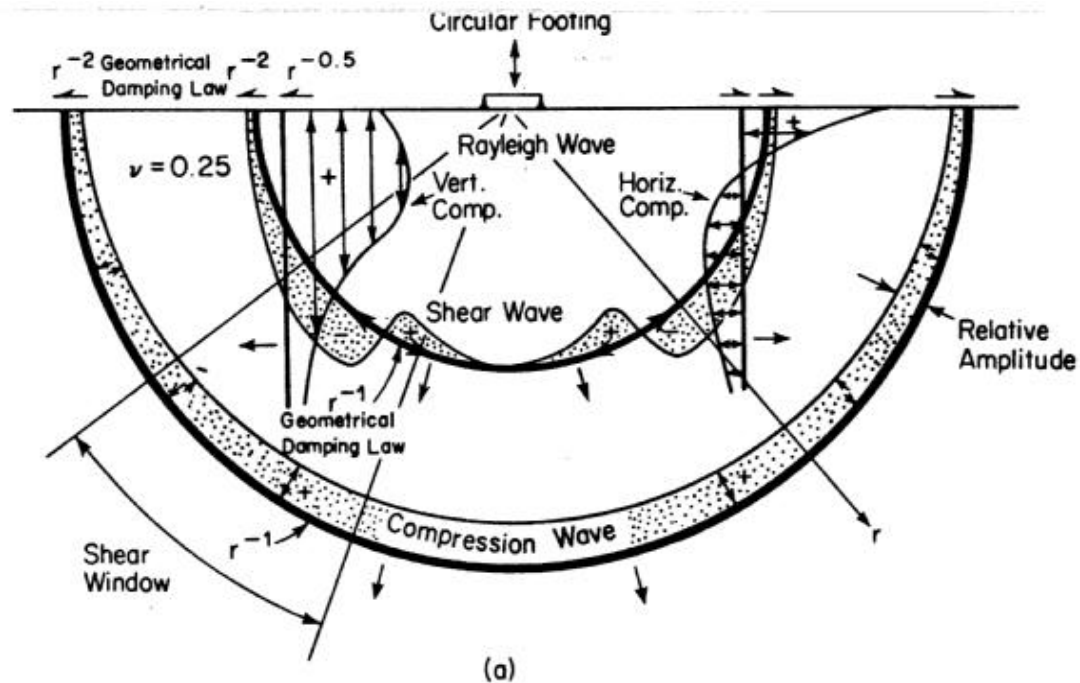
The impulsive or harmonic active point source creates a complex-valued, cylindrically spreading wavefield dominated by Rayleigh surface waves in the far-field. Traditional geotechnical analysis of surface waves has relied on several empirical and qualitative filtering requirements to minimize near-field effects. Numerical and analytical studies have shown that body waves may be significant in the near-field for up to two wavelengths (Tokimatsu, 1995; Lai, 1998; Sanchez-Salinero, 1987). The current section will briefly discuss the wavefield created by an active point source, the wave equations different types of waves satisfy, the significant physical difference between fundamental and additional mode Rayleigh waves, and the creation of additional mode Rayleigh waves. In some cases, the discussion remains intuitive and qualitative, but since geotechnical analysis of active point sources has never properly addressed some of the concerns, the brief discussion is necessary to highlight important aspects of seismic surface waves.

6.4.1 Seismic Energy Production and Partitioning

When an active point source inputs mechanical energy into the boundary of a homogeneous, isotropic, elastic half-space, the energy is partitioned into the fundamental Rayleigh wave mode, head waves, and compressive and shear body waves depending on the Poisson's ratio of the medium. The fundamental Rayleigh surface wave mode, created by the inability of reflected compressive waves to satisfy the stress-free boundary conditions at the surface of the earth for all angles below a critical incidence angle, exists solely due to the presence of the surface. The Poisson's ratio controls the value of the critical grazing

angle, and therefore, the Poisson's ratio determines how much energy is partitioned into the fundamental Rayleigh mode.

Figure 6.1 shows an often referenced study from Richart, Hall, and Woods (1970). For a Poisson's ratio $\nu = 0.25$ and a small circular load applied at the surface of the half-space, 67 percent of the energy goes into the fundamental Rayleigh mode, while only 26 percent and 7 percent go into the shear and compressive body wave modes, respectively. For a point source, geometric attenuation or spreading of energy plays an important role in the progression of the wavefield. The Rayleigh surface wave spreads cylindrically at a rate of $1/\sqrt{x}$ in the far-field, while the body waves spread spherically, at a rate of $1/x$ within the body of the half-space and at a rate of $1/x^2$ along the surface of the half-space. Due to the greater energy partitioned into the Rayleigh surface waves, and the much larger geometrical decrease in the body wave energy, actively produced seismic surface wavefields are dominated by Rayleigh surface waves.



Wave Type	Per Cent of Total Energy
Rayleigh	67
Shear	26
Compression	7

Figure 6.1 Partitioning of Seismic Energy for a Circular Dynamic Surface Load (From Richart, et al., 1970)

6.4.2 Seismic Wave Equations

A brief review of the wave equation solutions and geometric energy spreading will help clarify a few salient points concerning active source wavefields and allow an easier extension to the passive seismic energy source. Spherical wave propagation follows the following wave equation

$$s(x, t) = \frac{A}{x} e^{j(\omega t - kx)} \quad (6.1)$$

where $s(x, t)$ = displacement measured at spatial position x at time t and A = initial amplitude of the wave. Spherical wave propagation is symmetric, so the wave front depends only on the scalar distance x from the source and the scalar wavenumber k . Notice the $1/x$ amplitude decrease with increasing distance from the source x .

Cylindrical waves, on the other hand, follow a Hankel type solution, given by

$$s(x, t) = A H_0(kx) e^{-j\omega t} \quad (6.2)$$

where H_0 = the Hankel function of the first kind of order zero. The exponential term gives the motion harmonic time dependence. $H_0(kx)$ is given by

$$H_0(kx) = J_0(kx) + iY_0(kx) \quad (6.3)$$

where J_0 = the Bessel function of the first kind of order zero, and Y_0 = the Bessel function of the second kind of order zero. At fixed time $t = 0$, the real-valued motion due to the point source motion with amplitude A and frequency ω equals the real part of Equation 6.2, or

$$s(x, 0) = A J_0(kx) \quad (6.4)$$

Some salient and useful properties of the Bessel function are the following:

- 1.) The zeros of the Bessel function are unequally spaced. For $J_0(x)$, i.e. $k = 1$ and $\lambda = 2\pi$, the first zero occurs at $x = 2.405$, significantly larger than $\pi/2$, the first zero of a cosinusoid. The spacing of the zeros is largest near $x = 0$, and becomes more uniform, tending to π at large distances (Wallace, 1984),
- 2.) $J_0(0) = 1$,
- 3.) The Bessel functions have an oscillatory character, tending toward sinusoidal behavior at large distances,
- 4.) The Bessel function amplitude decays with increasing x , ultimately as \sqrt{x} (Elmore and Head, 1985),
- 5.) $J_0(kx)$ has an infinite number of real and simple zeros (Hochstadt, 1986),
- 6.) Denoting the positive zeros of J_0 by λ_k , the functions $\{ \sqrt{x} J_0(\lambda_k x) \}$ form an orthogonal set over the interval $(0, 1)$ (Hochstadt, 1986).

Property 1 will be important when discussing the model incompatibility effects on Rayleigh wave phase velocity estimates and optimum cylindrical beamforming. The orthogonality properties of Bessel functions will help illuminate the properties of cylindrical beamformers in relation to plane wave model estimators, and Property 4 will be important when considering the model incompatibility effects on attenuation estimation.

Traditional seismic surface wave analysis uses the far-field Hankel function approximations for both phase velocity estimation and energy attenuation. Neglecting waves decaying more rapidly than $1/\sqrt{x}$, the far-field (large kx) Hankel approximation can be given in several different forms, including the following presented by Wallace (1984)

$$H_0(kx) \approx \sqrt{\frac{2}{\pi kx}} \exp\left[i\left(kx - \frac{\pi}{4}\right)\right] \quad (6.5)$$

and, therefore, the real-valued Rayleigh surface wave vertical motions are given by

$$J_0(kx) \approx \sqrt{\frac{2}{\pi kx}} \cos\left(kx - \frac{\pi}{4}\right) \quad (6.6)$$

The horizontal motions associated with the Rayleigh surface wave are $\pi/2$ radians out of phase with the vertical motions in elastic media.

The asymptotic expansion of the Hankel function (Equation 6.5) clearly shows the $1/\sqrt{x}$ decay and plane wave nature of the cylindrical wave equation in the far-field. This chapter will discuss the effects of the far-field assumption on traditional geotechnical surface wave dispersion estimation from active sources, and Chapter 7 will discuss the effects of the far-field assumption on attenuation estimation.

6.4.3 A Note on the Production of Higher Mode Surface Waves

Significant difference exists between the creation of the fundamental Rayleigh surface wave mode and all additional Rayleigh modes. Although the properties of all modes, including exponential decay with depth, cylindrical spreading from a point source, and horizontal and vertical motion out of phase by $\pi/2$ radians in elastic media, are exactly the same, the additional Rayleigh modes are created from the reflection of body waves at the interface of layers. In the far-field, you could follow the ray path of all body waves produced by the point source, and the superposition of these waves would naturally create the additional modes. In fact, the method of reflection and transmission coefficients (Kennett, 1983) determines the eigenvalues (wavenumbers) of a layered soil profile through explicitly modeling the constructive interference of body wave modes. For the case of the fundamental Rayleigh mode, e.g. in a homogeneous half-space, no such interpretation of the interference of ray paths exists.

The Love wave example offers an analogue to the additional mode Rayleigh wave problem. Love waves are produced by the superposition of reflected horizontally polarized shear waves (SH) in a layered medium. In contrast to the case of Rayleigh waves, no fundamental Love mode exists in a homogeneous half-space, occurring only when the half-

space is covered by a layer of different material (Achenbach, 1984). This is a physically acceptable tenet, since the fundamental Rayleigh mode is due to the inability to satisfy the compression wave boundary conditions at the free surface. In the SH wave case, no critical angle of incidence exists because at all incidence angles the boundary conditions can be satisfied at a free boundary solely with the reflection of another SH wave. Just as in the case of additional mode Rayleigh waves, SH waves from a point source initially propagate out spherically, but after reflecting at the interface, superposition effects lead to surface wave behavior.

6.5 Spatiospectral Correlation Matrix and Synthetic Linear Arrays

The spatospectral correlation matrix $R(\omega)$ is estimated by combining the source-receiver cross power spectrum estimates for all spatial lags for a given frequency. Although the matrix does not have to be normalized, without normalizing, sensors at larger offsets would be effectively weighted less than near source lags due to geometric spreading of energy, since the magnitude of the cross power spectrum is less at larger offsets. Normalizing the matrix so all entries have a magnitude of one is not the only option available. As discussed in Section 6.6, multiplying by the square root of distance offers a better alternative for accounting for geometric spreading of energy.

The ability to combine several two-point spatial lag samples into one synthetic array relies on assumptions regarding the signal and noise characteristics. As shown in Chapter 4, the spatospectral correlation matrix may be broken into

$$R(\omega) = R_S(\omega) + R_N(\omega) \quad (6.7)$$

The use of a deterministic source with a linear, shift invariant soil profile model, allows $R_S(\omega)$ to be considered a constant matrix measured in an interfering noise background. Assuming the noise to be independent and identically Gaussian distributed at each sensor, the noise portion of the spatospectral correlation matrix may be written as

$$R_N(\omega) = I \mathbf{p}_n(\omega) \quad (6.8)$$

where I = the identity matrix, and \mathbf{p}_n = the noise power measured at each sensor as a function of frequency. Since each two-point measurement is obtained at different times, the noise background may not be stationary, i.e. the noise statistics may change during several measurements. Assuming the noise distribution is always Gaussian, the matrix may be refined as

$$R_N(\omega) = I \mathbf{p}_n(\omega) + \text{diag}\{p_i(\omega)\} \quad (6.9)$$

where the first term represents the noise power that is identical to all sensors, i.e. the minimum noise present in any sensor, and the second term is a diagonal matrix with the additional noise power unique to each sensor i . Since the active surface wave method uses a repeatable source, the previous assumptions about the noise statistics allow several two-point spectrums to be combined into a synthetic aperture. Combining several two-point

estimates into a single array greatly increases the resolution and sidelobe leakage control of the wavenumber spectrum estimators.

6.6 Accounting for Geometric Spreading of Energy

The Hankel transform offers a natural frame to discuss cylindrically symmetric seismic wavefield problems, since the Hankel function contains an asymptotic \sqrt{x} decay rate and solves the cylindrical wave equation. The Hankel transform of a function $f(x)$ equals

$$F(k) = 2\pi \int_0^{+\infty} f(x) J_0(kx) x dx \quad (6.10)$$

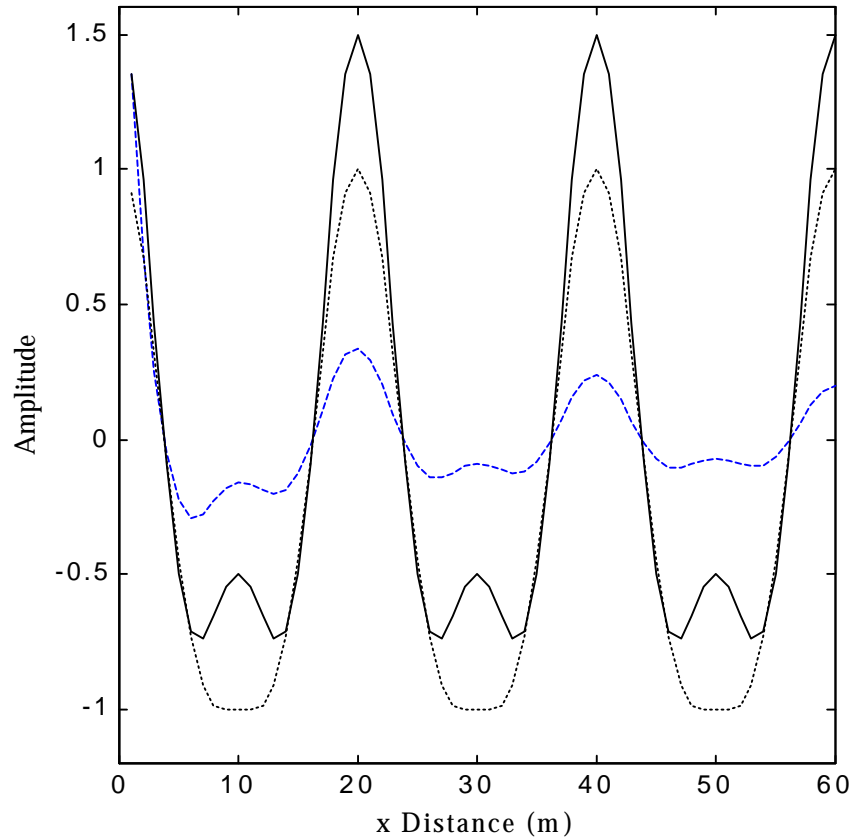


Figure 6.2 Wavefield at Frequency = 10 Hz Containing Two Modes and Decaying as $1/\sqrt{x}$. The motion contains the superposition of two modes, with velocities of 100 and 200 m/s and amplitudes of 0.5 and 1.0, respectively, spatially decaying as $1/\sqrt{x}$ (dashed line). The solid line normalizes the spatially decaying wavefield by \sqrt{x} . The dotted line normalizes the spatially decaying wavefield by dividing by the magnitude of the complex motion as a function of x , thus, normalizing the magnitude of the motion to one at all spatial locations.

where x = radial distance from the source, and the 2π in front of the integral accounts for the elemental area $2\pi x dx$ (Bracewell, 1986).

The geometric spreading of energy must be accounted for in the power spectrum estimator, otherwise, sensor measurements closer to the source will receive larger weights. Every manipulation of the experimental data will affect the final estimate, and the normalization for geometric spreading offers significant insight into the active power spectrum estimation problem. Two different normalization techniques and their effects on the power spectrum estimate will be discussed.

Figure 6.2 shows a wavefield consisting of two waves at a frequency = 10 Hz. The wave velocities are 100 and 200 m/s, with amplitudes of 0.5 and 1.0, respectively. For illustration purposes, the wavefield decays at a rate $= 1/\sqrt{x}$. The dotted line shows normalization of the wavefield to a magnitude of one, while the solid line multiplies the wavefield by \sqrt{x} . Notice the effects of the different normalization techniques.

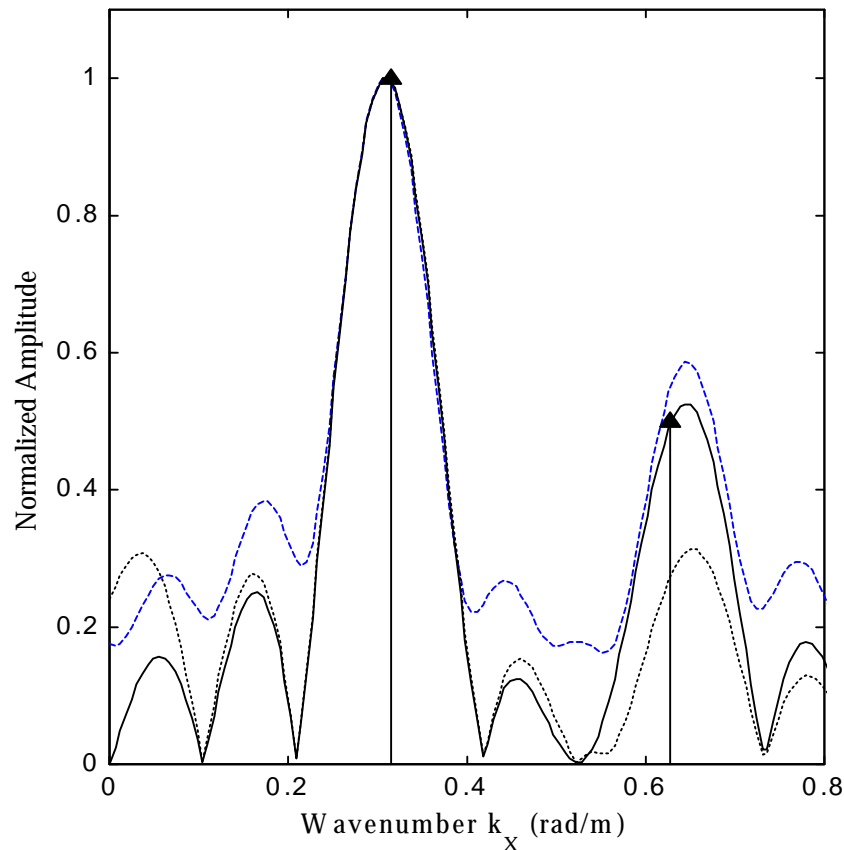


Figure 6.3 Steered Response for the Three Waves Shown in Figure 6.2. Notice that the wave multiplied by \sqrt{x} exhibits the best amplitude estimate for the mode with a lower amplitude. The line types are the same as used in Figure 6.2.

Normalizing the measured magnitudes to one significantly reduces the ripple near the minimums of the measurements, while multiplying by \sqrt{x} tends to emphasize the ripples.

The effects in the spatial domain measurements are emphasized when transformed into the wavenumber spectral domain. Figure 6.3 shows the wavenumber spectrum for the wavefields shown in Figure 6.2. Although all three of the wavefields yield approximately correct peak locations, the wavefield multiplied by \sqrt{x} yields peak heights closest to the correct energy content. Two additional features of Figure 6.3 recommend multiplying the wavefield by \sqrt{x} . First, the smaller peak for the wave normalized to unity magnitude is approximately the same height as the sidelobe near wavenumber = 0.05 rad/m. Second, the wavefield multiplied by \sqrt{x} seems to offer the greatest sidelobe and background energy control.

6.7 Multiple Signals, Resolution, and Bias

Seismic surface wave problems encountered in geotechnical engineering typically contain multiple signals, for example separate signals propagating from different directions,

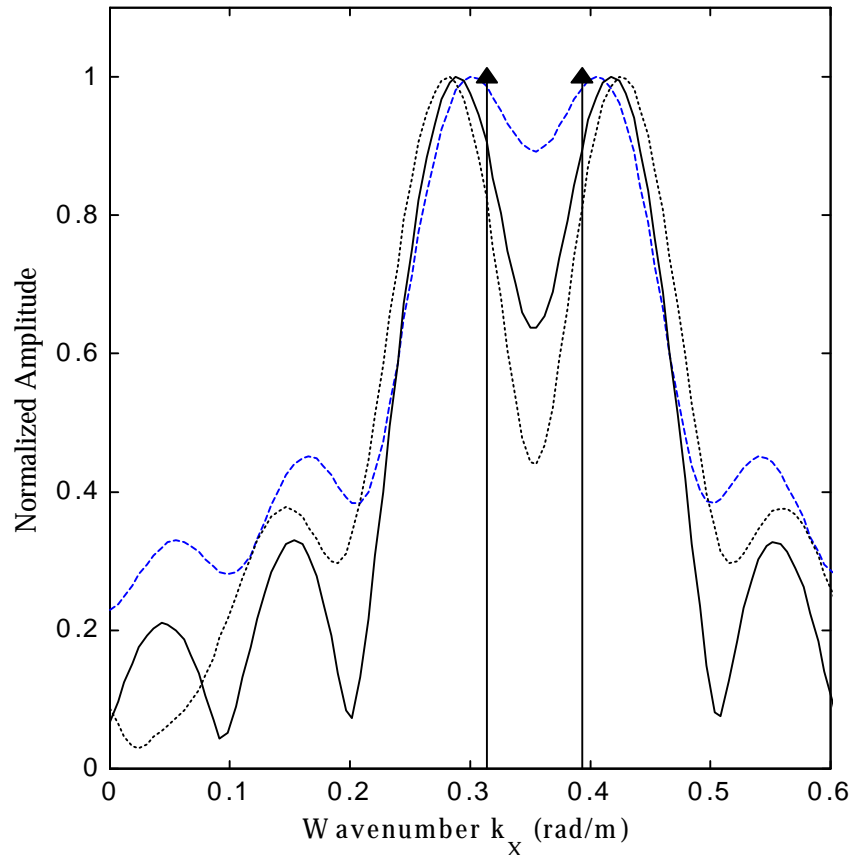


Figure 6.4 Steered Response for Frequency = 10 Hz, Two Modes with Amplitude Equal to 1 and Velocities Equal to 160 and 200 m/s

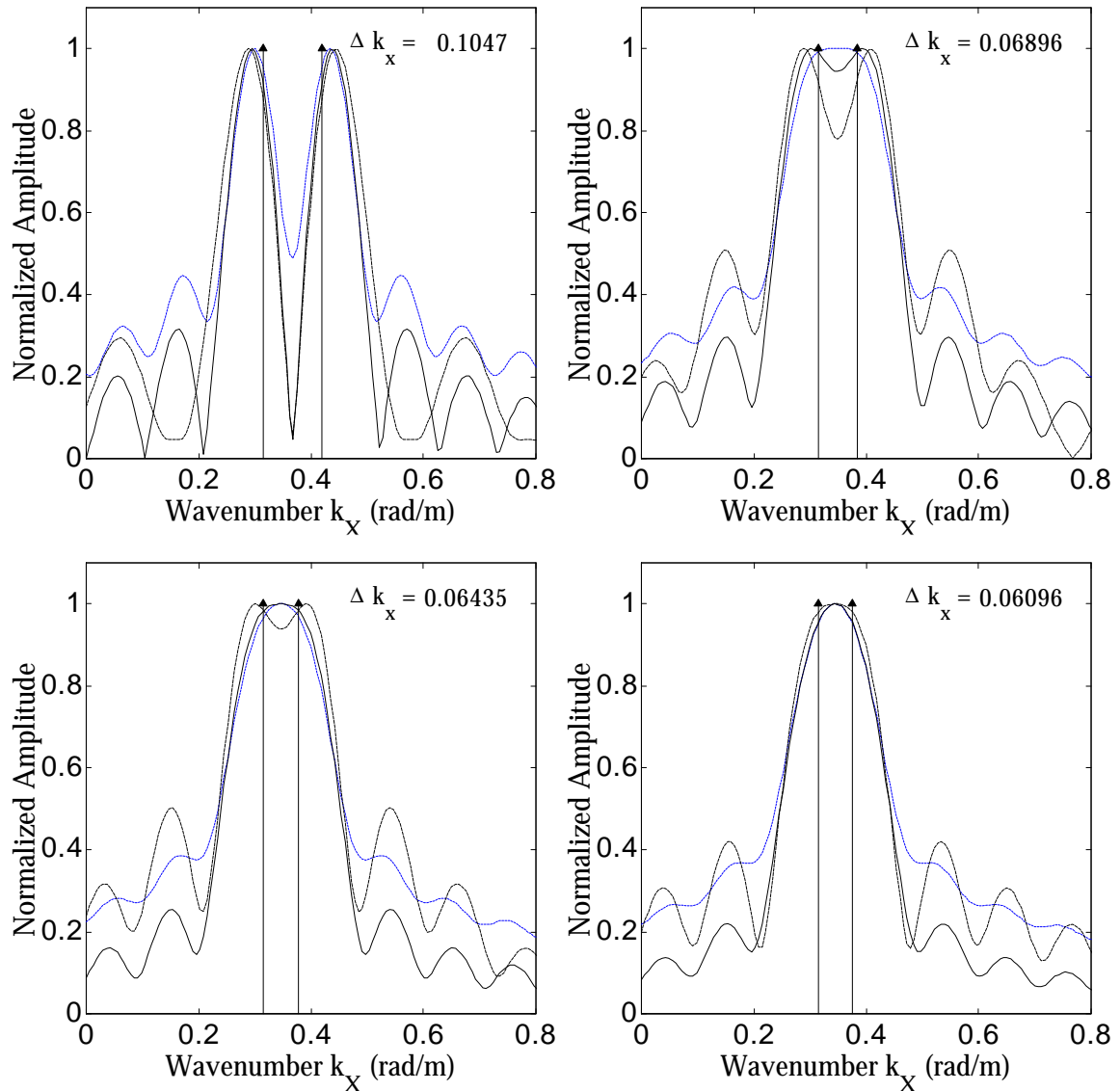


Figure 6.5 Array Resolution for Different Spatial Displacement Normalization Techniques. Two waves, with amplitudes equal to one, propagate past the array with progressively closer wavenumber spacing. The results from using no normalization technique (solid line), multiplying the wavefield by \sqrt{x} (dashed line), and normalizing the magnitude of displacements to one (dotted line) are shown.

multipath, or multiple modes propagating at the same frequency with different velocities. The presence of multiple signals introduces several concerns into the spectrum estimation problem, including bias of direction and velocity estimation, sidelobe masking of weak signals, and resolution.

Figure 6.4 shows the wavenumber spectrum estimate for a wavefield containing two equal amplitude signals propagating with velocities equal to 160 and 200 m/s. The line

types are the same as shown in Figure 6.3. As resolution due to different normalization techniques increases, measured by decreasing width of peaks, the bias of the peak locations increases. The unnormalized signal shows the least resolution, but the peak locations are closer to the correct signal locations. As in Figure 6.3, the signal multiplied by \sqrt{x} displays the greatest sidelobe control.

The ISC '98 synthetic linear array (discussed in the next section) has a maximum spatial lag equal to 60 m, and the classical resolution criterion discussed in Chapter 3 equals

$$\text{Classical Resolution} \approx \frac{2\pi}{\text{Array Length}} = \frac{2\pi}{60 \text{ m}} = 0.105 \frac{\text{rad}}{\text{m}} \quad (6.11)$$

Depending on the normalization of the measured cylindrical wavefield, the resolution of the array measurements actually will be better than the classical criterion. Figure 6.5 shows a series of spectrums produced from wavefields containing two signals with progressively closer wavenumber separation. Although the classical resolution equals 0.105 rad/m, the unnormalized wavefield spectrum resolves the two signals to a signal separation of 0.069 rad/m. Multiplying the wavefield by \sqrt{x} , the spectrum estimate resolves the two signals down to a separation equal to 0.064 rad/m, and normalizing the magnitude to unity resolves

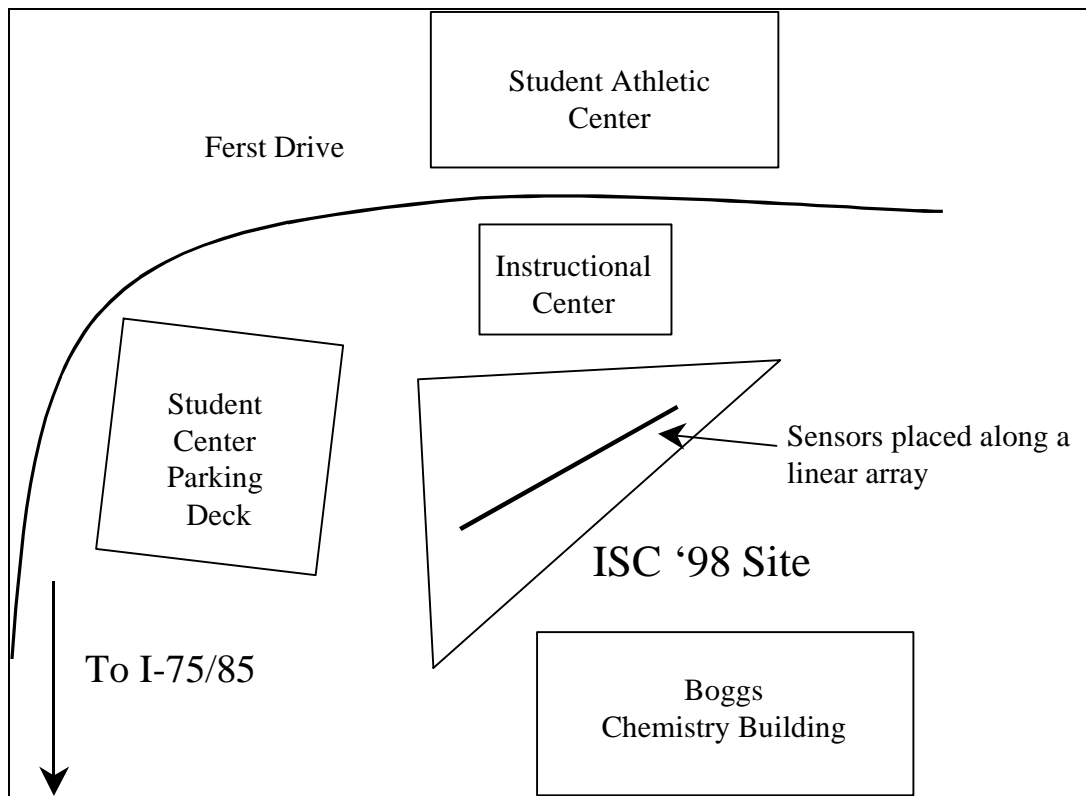


Figure 6.6 Schematic of ISC '98 Site and Position of Linear Array

the signals down to a separation of 0.061 rad/m. In Figure 6.5, the bias of the different estimates and the better sidelobe control of multiplying by \sqrt{x} is once again evident.

6.8 International Conference on Site Characterization Site (ISC '98 Site)

The First International Conference on Site Characterization was held in 1998 in Atlanta, GA. A test site on the campus of the Georgia Institute of Technology was chosen for extensive determination of the near-surface earth material properties. Active SASW tests were conducted to determine the near surface dynamic properties of the site. A schematic of the site and the location of the measurements are shown in Figure 6.6. A typical soil profile in this area consists of residual silty sands and sandy silts overlying partially weathered and intact rock (gneiss and schist). The shear wave velocities generally increase with depth as the amount of weathering decreases (Zywicki and Rix, 1999).

Since a deterministic, repeatable source is used, the measurements taken at different lags can be combined to yield a synthetic array, as discussed in Section 6.5. The ISC '98 synthetic array consists of 15 two-point measurements, covering lag distances from 1 m to 60 m. Figure 6.7 shows the synthetic array and the corresponding array smoothing function. Notice the locations of the sidelobes at wavenumbers around 1.2 and 2.5 rad/m.

6.9 Plane Wave Multidimensional Power Spectrum Estimation

The frequency-wavenumber spectrum estimation methods discussed in Chapter 4 utilize a plane wave model. Although the active seismic wavefield is cylindrical, the plane wave methods offer computational advantages over the cylindrical estimators covered later, since the Fast Fourier Transform (FFT) can be utilized in the spectrum estimation algorithm (see Appendix A).

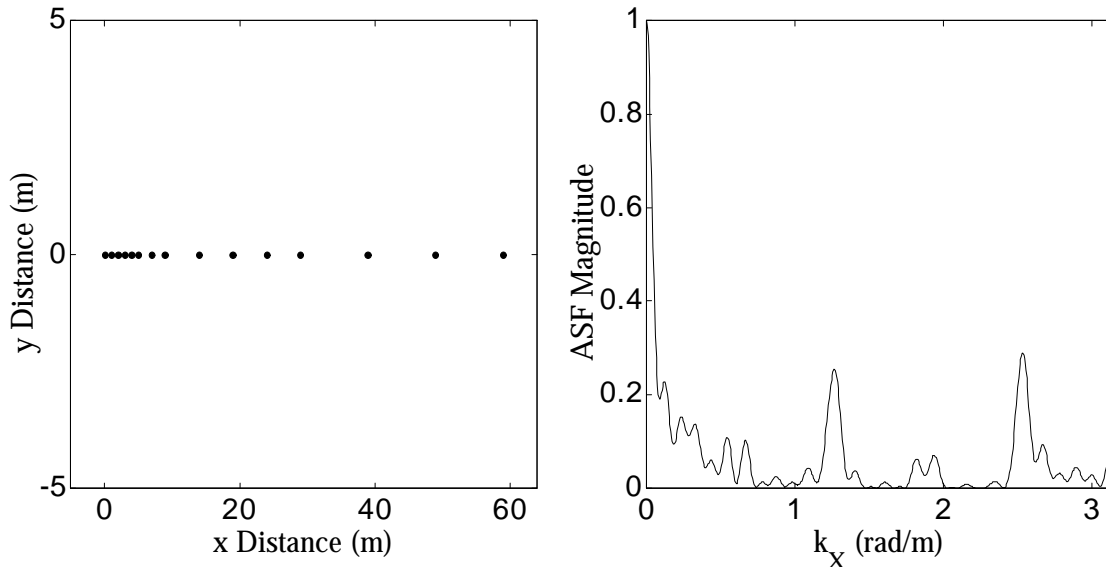


Figure 6.7 ISC '98 Synthetic Linear Array (left panel) and Array Smoothing Function (right panel)

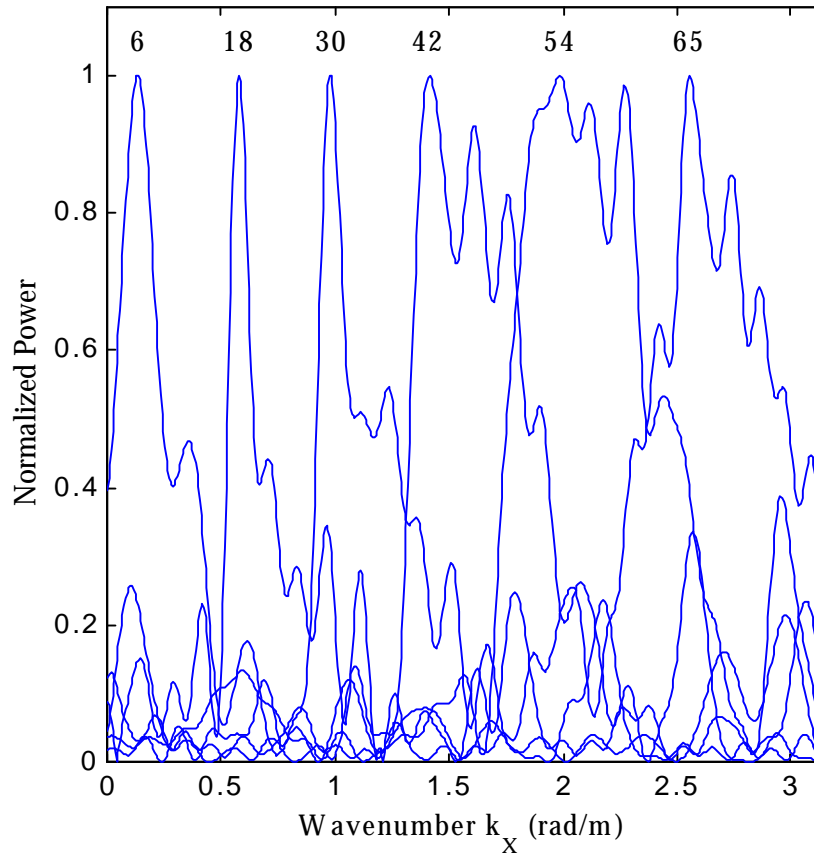


Figure 6.8 Progression of FDBF Wavenumber Power Spectrum Estimates as Frequency Increases from 6 Hz to 65 Hz

6.9.1 Conventional FDBF

The results of applying the conventional FDBF to the ISC '98 experimental data are shown in Figures 6.8 to 6.14. The progression of the FDBF power spectrum estimates from 6 Hz to 65 Hz is shown in Figure 6.8. Several modes appear to be present, especially at higher frequencies. Figure 6.9 shows the FDBF power spectrum estimate for several individual frequencies. The traditional two-point cross power spectrum and transfer function estimators are shown for reference with an asterisk and a circle, respectively. The spectrums contain sidelobes approximating the expected 0.2 height, and the three higher frequencies contain energy spread over several modes. The energy spread is emphasized in Figure 6.10, which plots the power spectrum for frequency = 52.5 Hz on a dB scale. The traditional transfer function method tends to overestimate the peak energy wavenumber, while the traditional cross power spectrum method tends to underestimate the peak energy wavenumber.

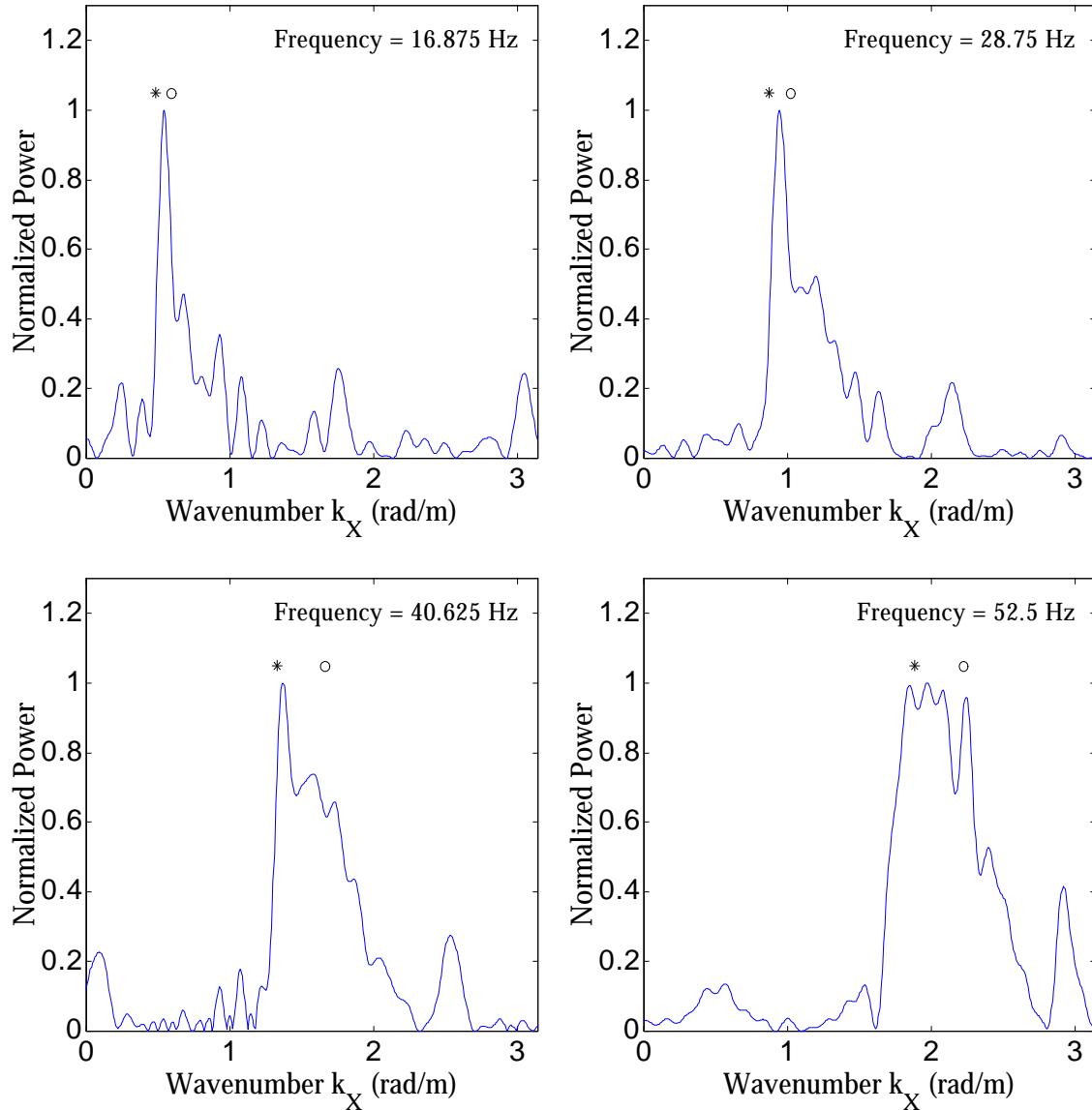


Figure 6.9 Four FDBF Power Spectrum Estimates on a Linear Scale to Emphasize Peaks. The traditional cross power (asterisk) and transfer function (circle) estimates are shown for reference.

The complete dominant mode dispersion curve estimate for the ISC '98 site is shown in Figure 6.11. The traditional two-point dispersion curve estimates are shown for reference. Figure 6.12 shows a closer view of the dispersion curve, emphasizing the difference between the traditional and conventional methods and the presence of several modes. The traditional assumption that the fundamental mode dominates the dispersion curve in normally dispersive media appears to require reconsideration. In this case, the traditional estimates tend to bound the FDBF dispersion curve. The FDBF allows the phase velocity to be estimated down to around 5 Hz, corresponding to wavelengths around 160

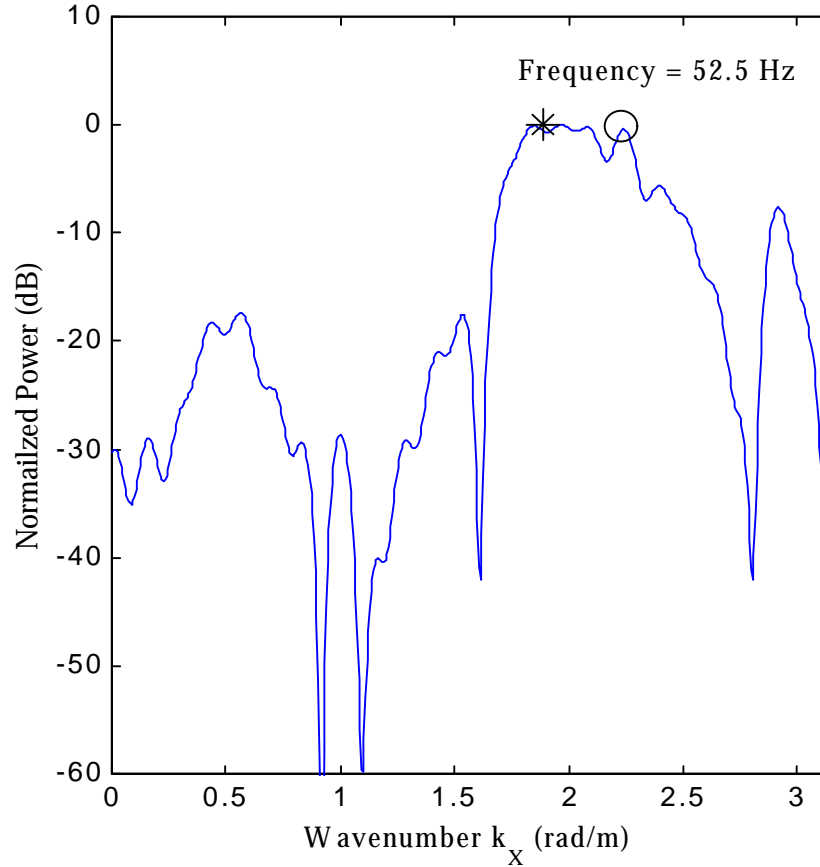


Figure 6.10 FDBF Power Spectrum Estimate at a Frequency = 52.5 Hz Plotted on a dB Scale. The asterisk and circle show the traditional cross power and transfer function estimates, respectively.

m. The array-based FDBF allows longer wavelengths to be estimated due to two reasons: 1.) The longer spatial distance contained in the array minimizes the model incompatibility effects near the source, and 2.) The FDBF filters out a single wavenumber. Since the array has a limited length, the resolution suffers as the wavelength increases, and therefore, the phase velocity estimates at lower frequencies probably correspond to a mix of modes. The discontinuity near 10 Hz probably is due to the inability of the array to resolve separate modes near 10 Hz. Above about 12 Hz, the array appears to have isolated four separate modes, and the phase velocity estimates below about 8 Hz fit the trend appearing after about 12 Hz.

Figure 6.13 shows a plot of the FDBF frequency-wavenumber power spectrum estimate. Separate modes and sidelobes are easily seen. To emphasize the problem of sidelobe control encountered with fixed array smoothing functions, Figure 6.14 plots the FDBF power spectrum estimate for frequencies from 6.07 Hz to 7.85 Hz. Constant amplitude and identically spaced sidelobes are persistently present as the smoothing function

slides across wavenumber space. One of the primary goals of the more advanced estimation methods is to minimize the effects of sidelobes in the array spectral smoothing function.

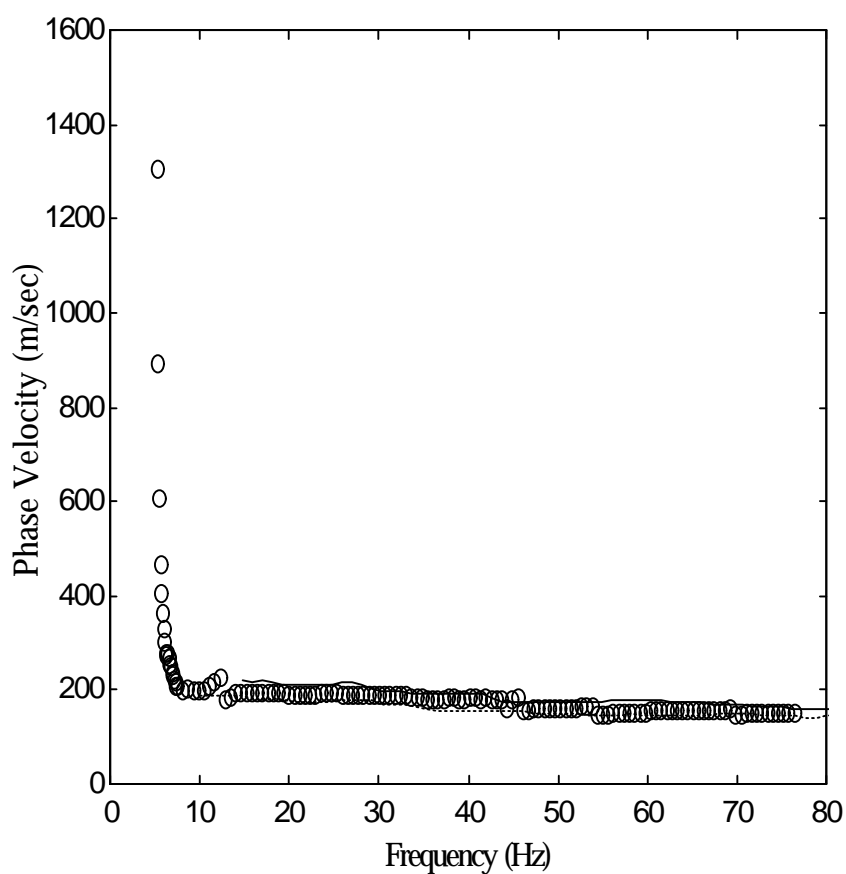


Figure 6.11 FDBF Dispersion Curve (plotted with circles). The traditional two-point cross power (solid line) and transfer function (dashed line) dispersion curve estimates are plotted for reference.

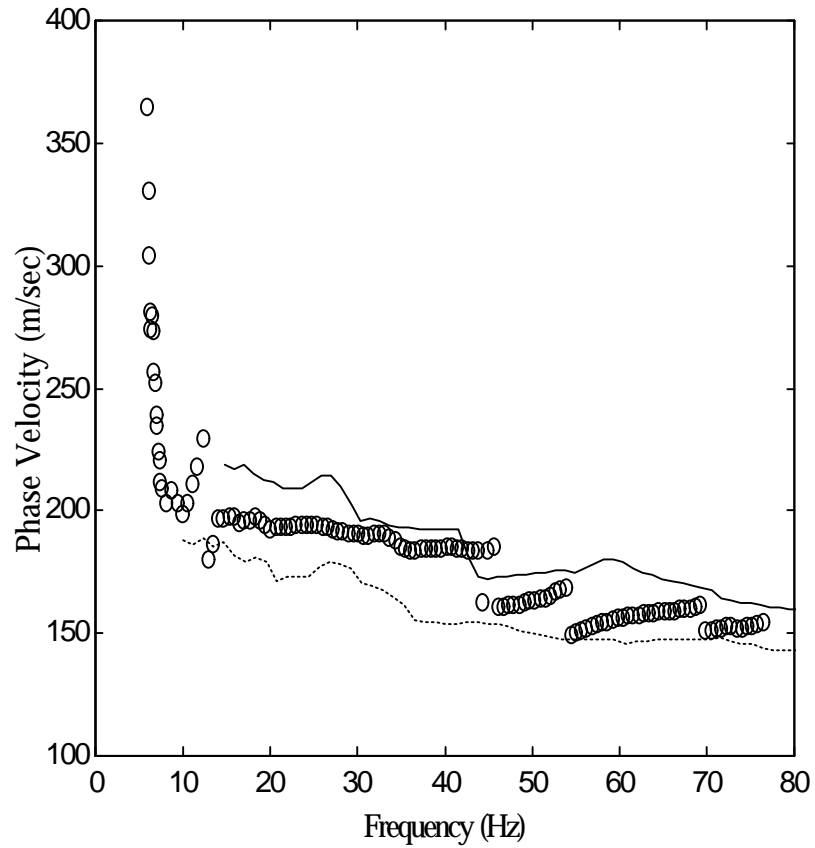


Figure 6.12 Close Up of Figure 6.11 to Emphasize Trends of Phase Velocity Estimates. The conventional FDBF dispersion curve (plotted with circles), the traditional two-point cross power spectrum (solid line), and transfer function (dashed line) dispersion curve estimates are shown.

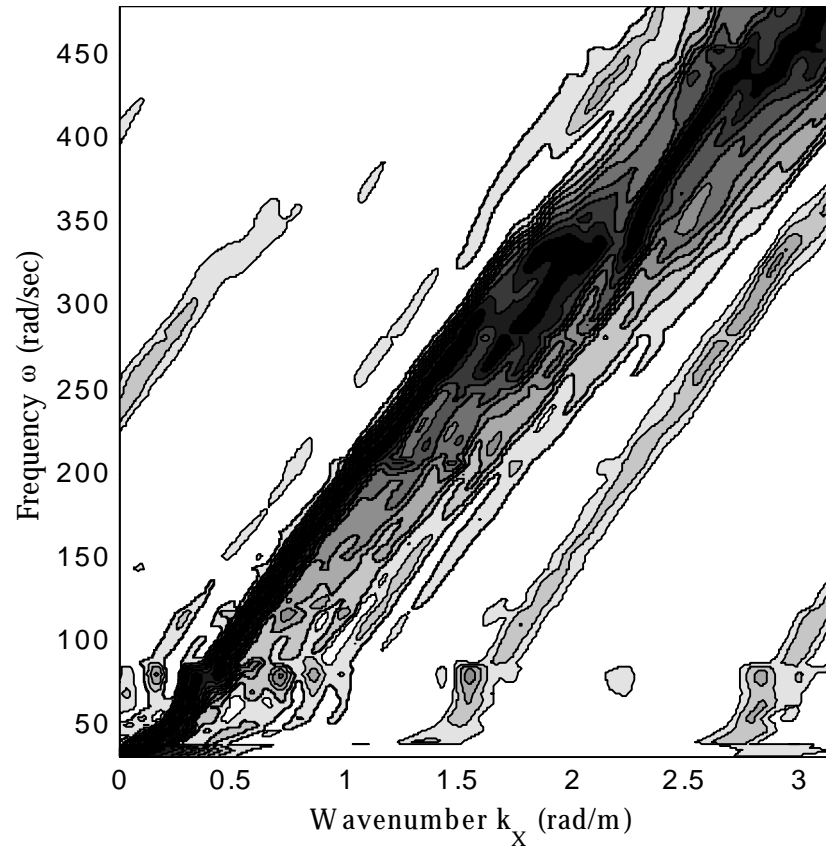


Figure 6.13 FDBF Power Spectrum Estimate as a Function of Temporal Frequency and Wavenumber. Darker areas indicate larger power estimates.

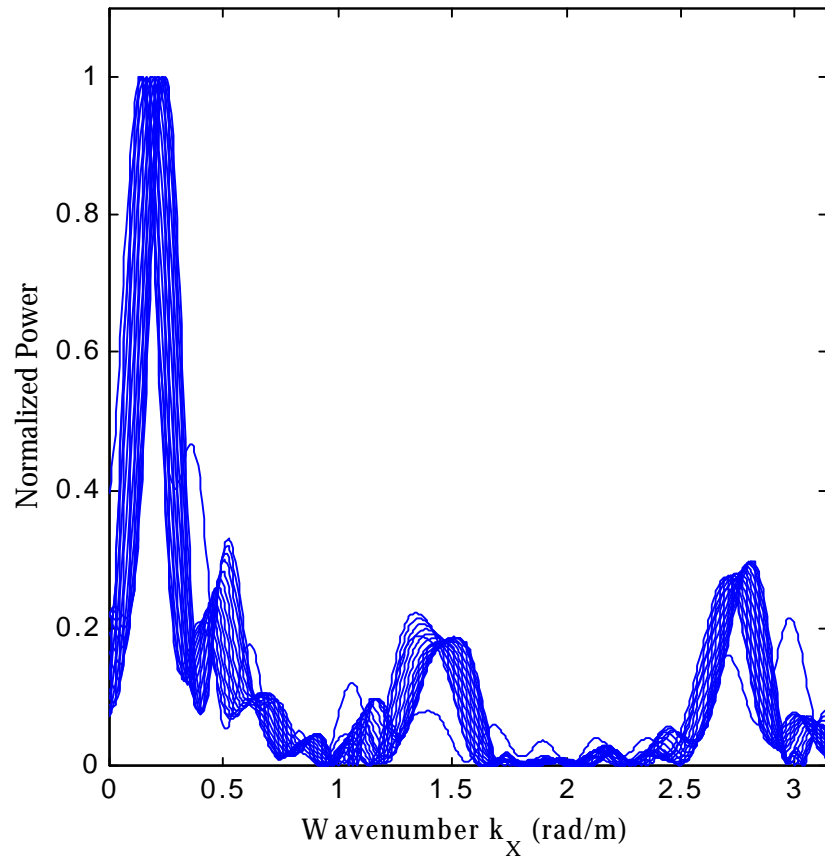


Figure 6.14 FDBF Power Spectrum Estimates for Frequencies from 6.0687 to 7.85 Hz. Notice the clearly distinguished and persistent sidelobes, with heights as expected from the array smoothing function shown in Figure 6.7.

6.9.2 Capon's MVDL

The results of applying Capon's MVDL method to the ISC '98 experimental data are shown in Figures 6.15 to 6.17. Figure 6.15 shows the MVDL power spectrum estimate for a few frequencies. Compared to the FDBF estimate, the MVDL exhibits narrower signal related peaks, smoother background power, and much greater sidelobe control. Figure 6.16 shows the dispersion relation estimate from the MVDL method. The MVDL and FDBF estimates are almost identical, which would be expected for a low noise environment. Figure 6.17 shows the overall power spectrum estimate for all frequencies in plan view. Notice the much narrower signal related darker area than for the FDBF. In addition, no persistent sidelobes are present in the MVDL estimate.

The magnitude and complex-valued weights for the frequency = 28.75 Hz are shown in Figure 6.18. The weights are shown for two directions to display the adaptive nature of the MVDL method. The smoothing function for the MVDL focused on a wavenumber other than the one associated with the dominant signal is shown in Figure 6.19, and the FDBF smoothing function is shown for reference. The MVDL method has altered the structure of the nulls and sidelobes, attempting to place a null in the direction of the competing signal. The MVDL has sacrificed sidelobe height in exchange for a decrease in the energy leakage from the signal remote from the wavenumber of interest.

Multipath is an important concern when using MVDL. Since MVDL attempts to null out competing signals, closely spaced signals arriving due to multipath may cause unexpected results. The close proximity of the nulled signal may cause the MVDL method to design a filter that cancels out the signal of interest as well.

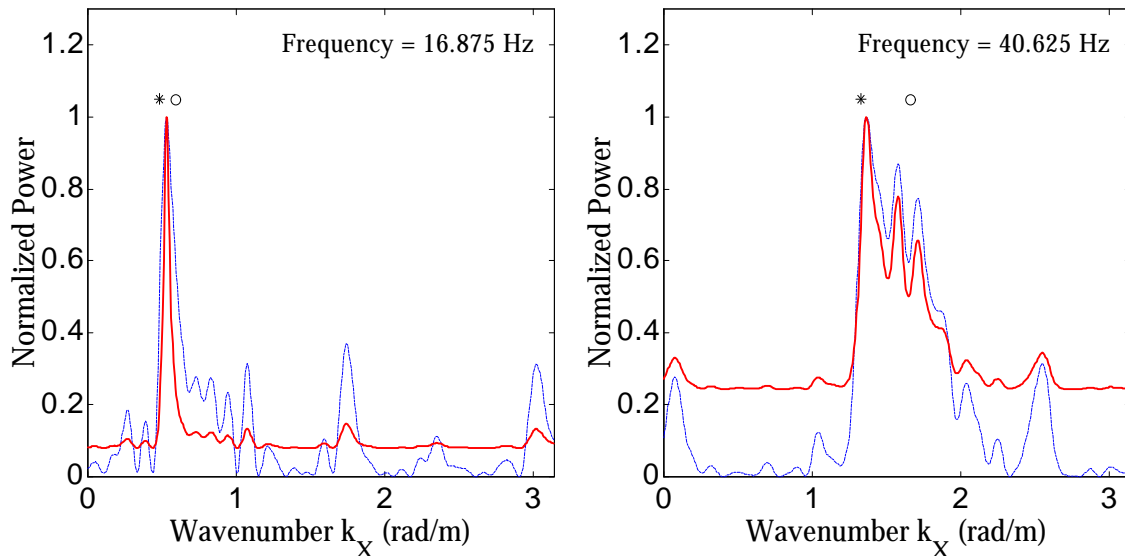


Figure 6.15 MVDL Power Spectrum Estimates. The MVDL estimates are shown in solid line, with the FDBF power spectrum estimate (in dashed) shown for reference.

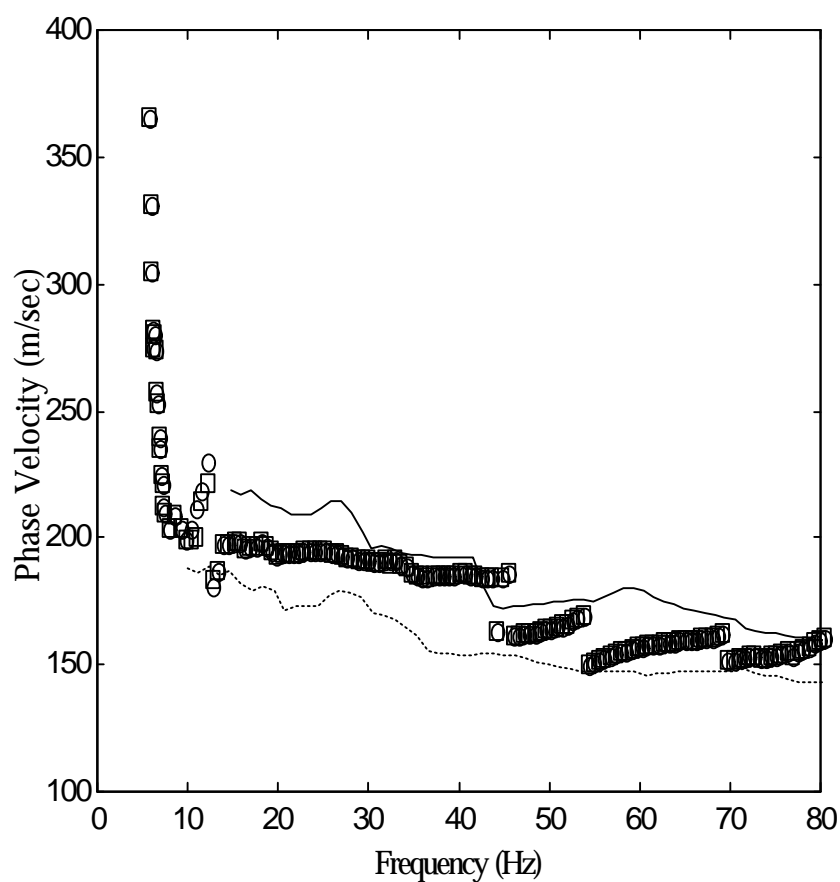


Figure 6.16 MVDL Dispersion Curve Estimate. The MVDL dispersion curve estimate (squares) is shown, with the FDBF dispersion curve (circles), traditional two-point cross power spectrum (solid line), and transfer function (dashed line) methods shown for reference.

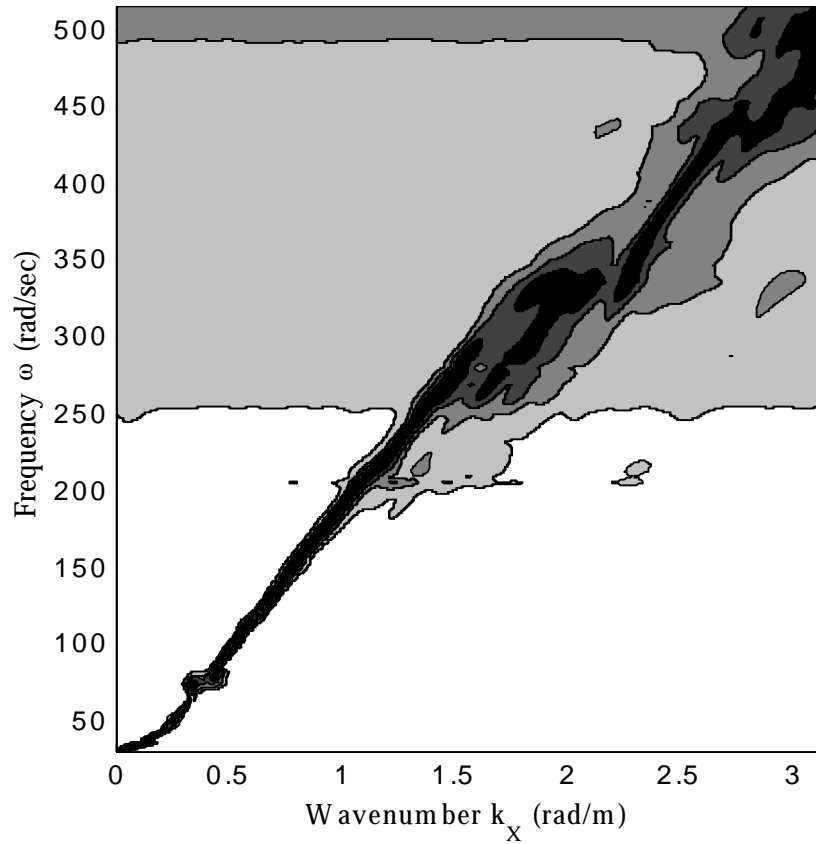


Figure 6.17 MVDL Power Spectrum Estimate as a Function of Temporal Frequency and Wavenumber

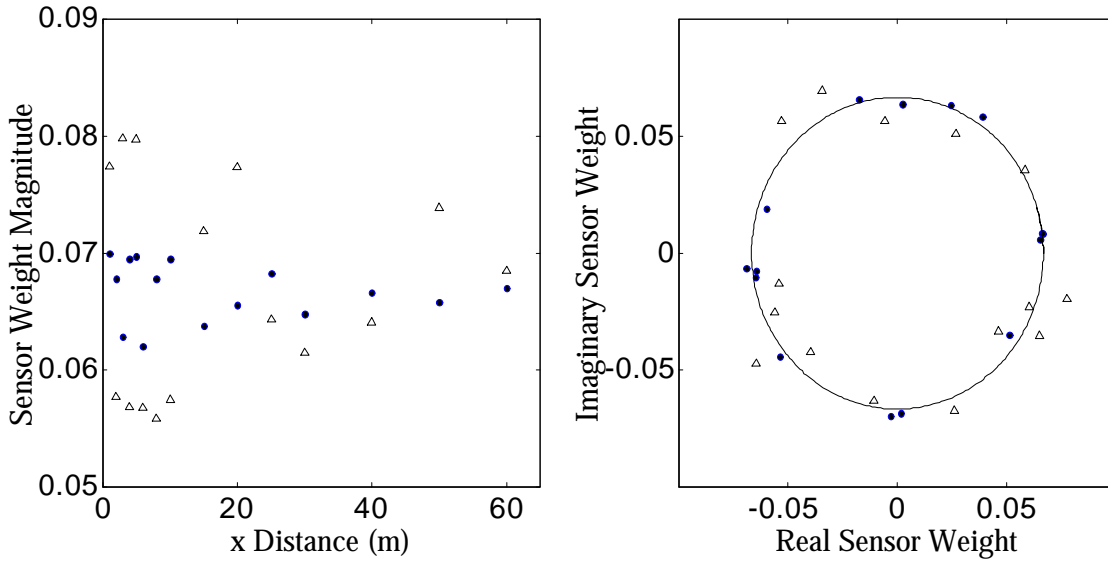


Figure 6.18 Minimum Variance Distortionless Look Magnitude (left panel) and Complex-Valued (right panel) Sensor Weights for Frequency = 28.75 Hz. The weights are shown for the cases of looking in the direction of the dominant wave, $k = 0.944$ rad/m (shown with circles), and in another direction, $k = 2.0$ rad/m (shown with triangles). In the right panel, a constant magnitude circle with the average weight is shown for reference.

6.9.3 Linear Prediction

The results of applying the linear prediction method to the ISC '98 experimental data are shown in Figures 6.20-6.23 and 6.25. Figure 6.20 shows several power spectrum estimates when using sensor number 3 as the reference sensor. In some cases, linear prediction produces much narrower signal related peaks and predicts peaks at a mode different from the FDBF peak location. The power spectrum estimates also exhibit linear prediction's greater ability to control sidelobes.

As discussed in Chapter 4, linear prediction estimates depend on the choice of reference sensor. Figure 6.21 shows two spectrum estimates using sensor 10 as the reference. The power spectrum estimates differ from Figure 6.20, and in the case of frequency = 64.375 Hz, the peak has moved. Figure 6.22 shows a plan view of the linear prediction power spectrum estimate using sensor 12 as the reference. The method appears to have isolated several modes, but persistent sidelobe ripple is also present. Figure 6.23 shows the optimum magnitude and complex-valued weights calculated using linear prediction for a frequency = 18.42 Hz and sensor 10 as the reference.

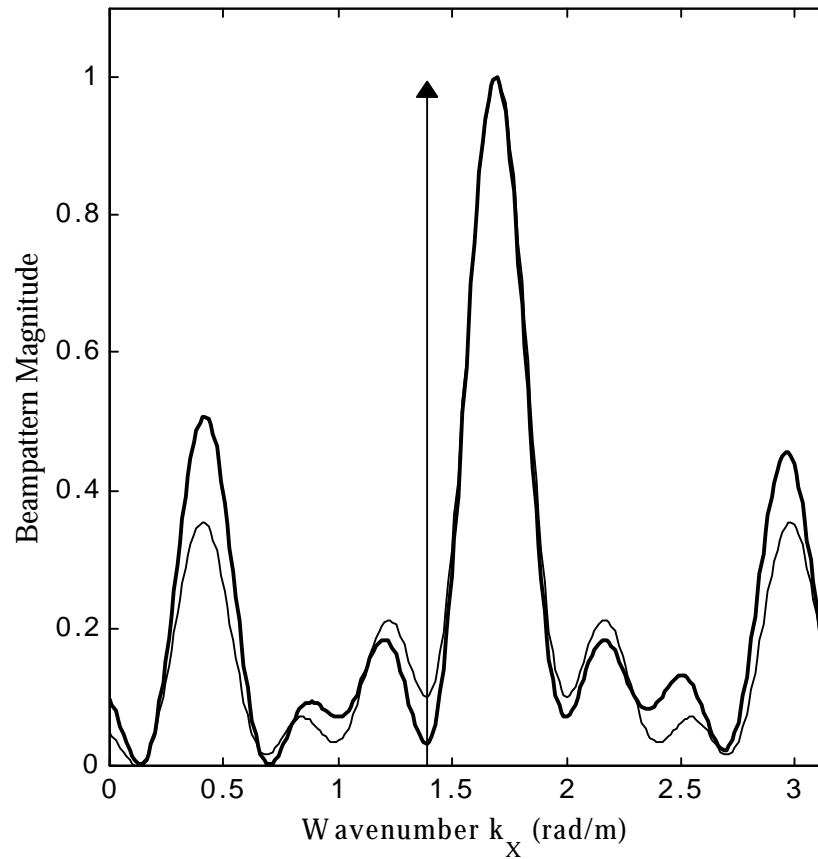


Figure 6.19 Adaptive Properties of the MVDL Method. The beampattern for the MVDL method, for a frequency = 40.62 Hz, when steered in a direction corresponding to $k_x = 1.70$ rad/m and the dominant signal is propagating with a $k_x = 1.38$ rad/m is shown in the dark line. The FDBF (light line) constant smoothing function centered on the look direction is shown for reference. In exchange for increased sidelobe height, the MVDL method attempts to place a null at the wavenumber containing energy. Only sensors 5 to 10 were used to emphasize the adaptation.

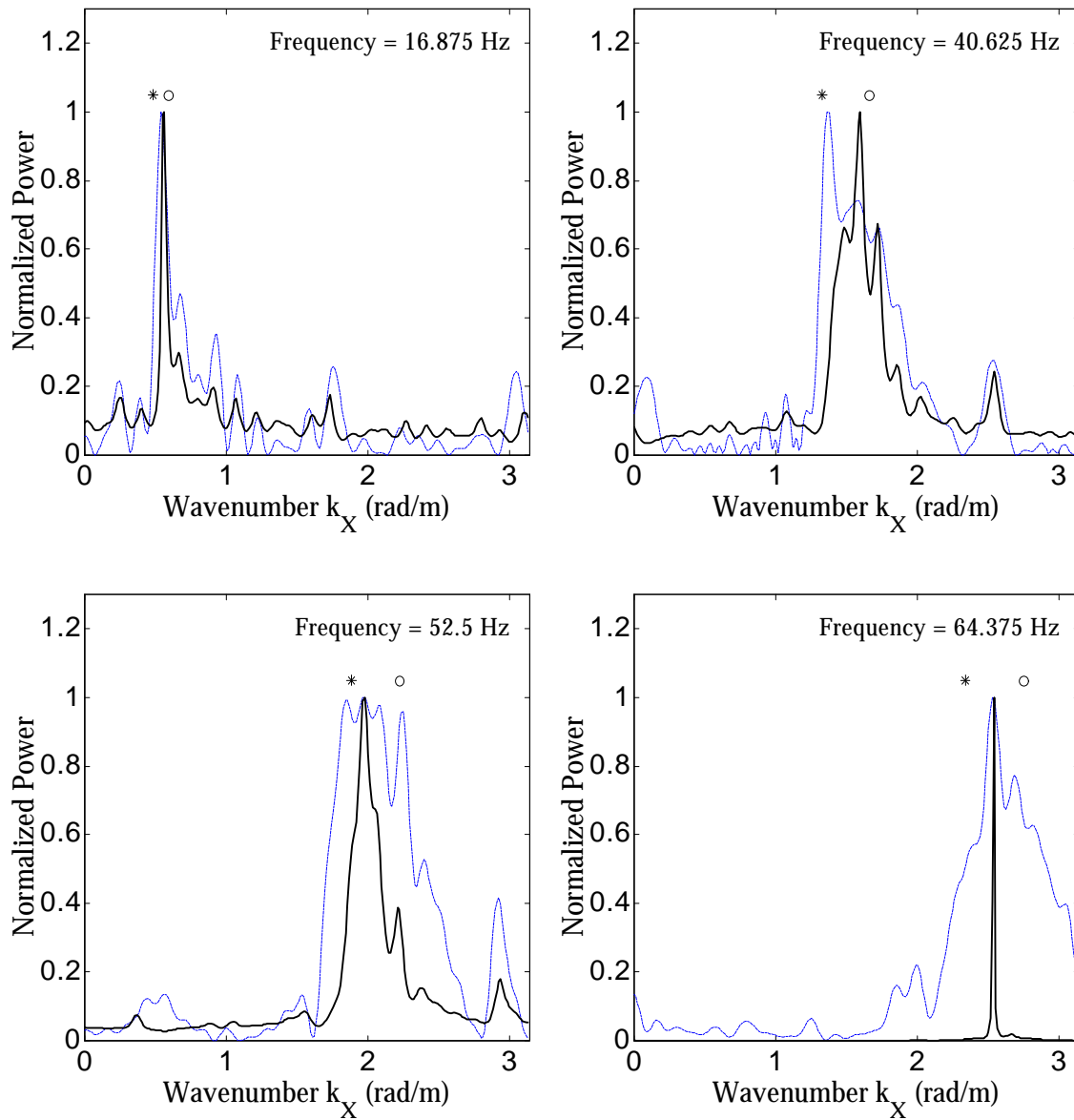


Figure 6.20 Linear Prediction Power Spectrum Estimates. The linear prediction power spectrum estimates using sensor position three for reference are shown in the solid lines. The FDBF power spectrum estimates are shown with dashed lines for reference.

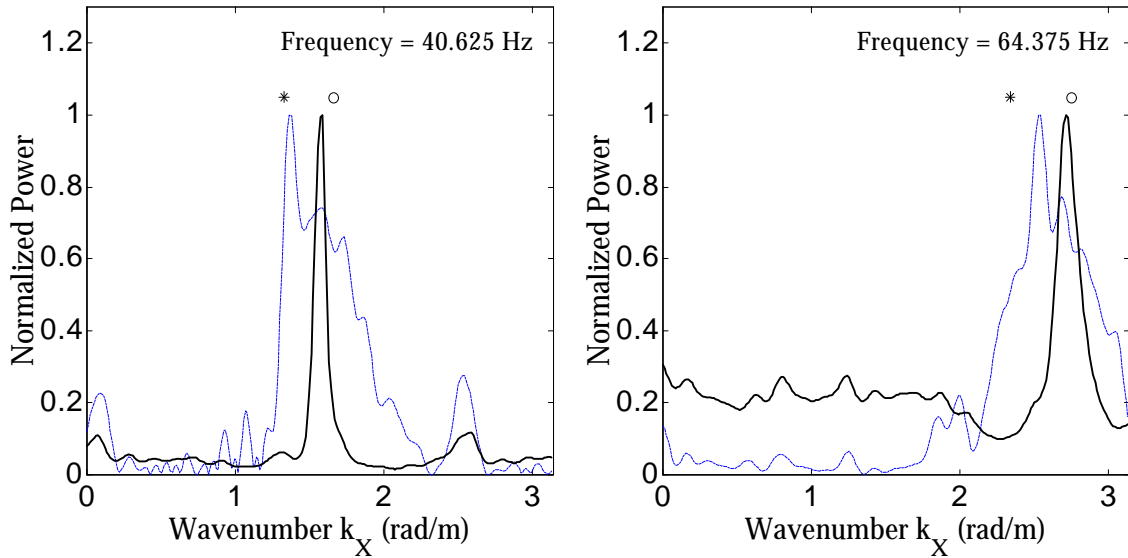


Figure 6.21 Linear Prediction Power Spectrum Estimates Using Sensor 10 as the Reference Position. The linear prediction power spectrum estimates (solid line) and the FDBF estimates (dashed lines) are shown for two frequencies.

The dispersion curve determined with linear prediction and sensor 12 as the reference is shown in Figure 6.25. As discussed in Chapter 4, the performance of linear prediction may deteriorate in multiple signal and additive noise environments. Using sensor 12 as the reference produced good results, but some other reference positions produced biased and poor estimates compared to FDBF. Advanced linear prediction methods exist that attempt to reduce the possibility of bias. See Hayes (1996) for possible alternatives.

6.9.4 MUSIC

The results of applying MUSIC to the ISC '98 experimental data are shown in Figures 6.24 and 6.26-6.27. Figure 6.24 shows the MUSIC power spectrum estimates for two frequencies. The MUSIC method offers a narrower signal related peak at 16.875 Hz compared to the FDBF. At a frequency = 40.625 Hz, and a larger signal subspace dimension, MUSIC has stronger signal related peaks, but the spectrum estimate also suffers from several spurious peaks. Figures 6.26 and 6.27 show the MUSIC estimated dispersion curve and a plan view of the frequency-wavenumber power spectrum estimate.

6.9.5 Comparison

The estimated dispersion curves from the conventional and adaptive signal processing methods are very similar, which is expected due to the use of a repeatable source in a relatively high signal-to-noise environment. The MVDL and MUSIC methods yield much narrower signal related peaks compared to the FDBF, and the larger sidelobes and mainlobe of the FDBF are easily seen. The wavenumber estimates from the two-point traditional estimators differ from the conventional and adaptive estimators considerably. In

the normally dispersive case presented, i.e. a generally increasing velocity with increasing wavelength, the transfer function and cross power spectrum traditional estimators seem to bound the more advanced phase velocity estimates. The traditional estimator “bounding” results will be discussed in Section 6.14. The linear prediction method yielded good results using sensor 12 as the reference, but other reference positions produced biased dispersion curve estimates. Multipath is an important consideration when using adaptive estimators.

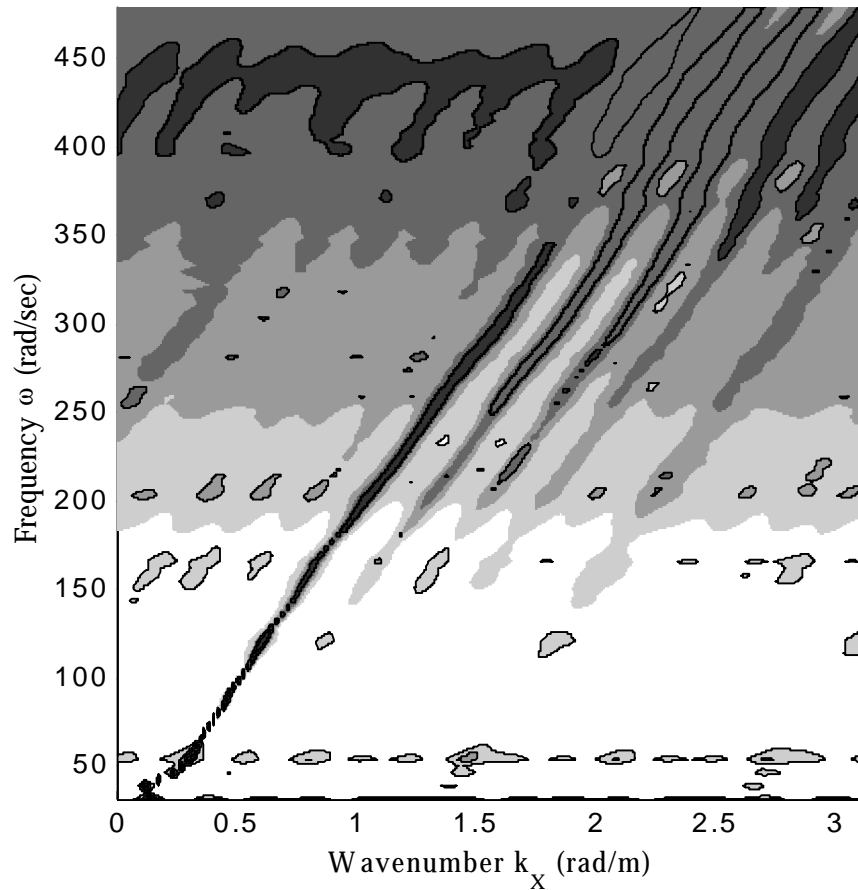


Figure 6.22 Linear Prediction Power Spectrum Estimate as a Function of Temporal Frequency and Wavenumber. Sensor 12 was used as the reference position.

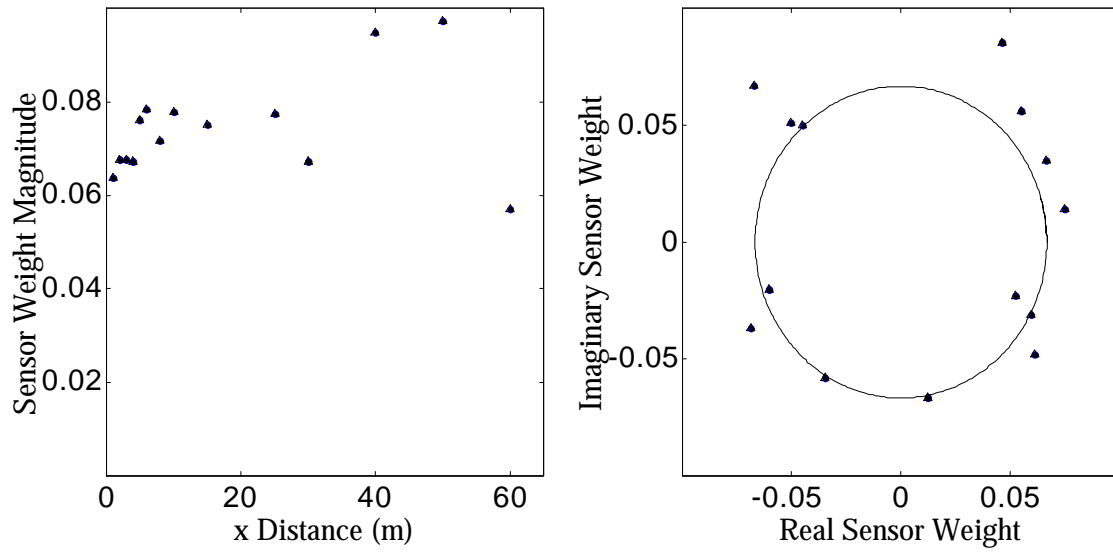


Figure 6.23 Magnitude (left panel) and Complex-Valued (right panel) Linear Prediction Weights at a Frequency = 18.42 Hz when Using Sensor 10 as the Reference

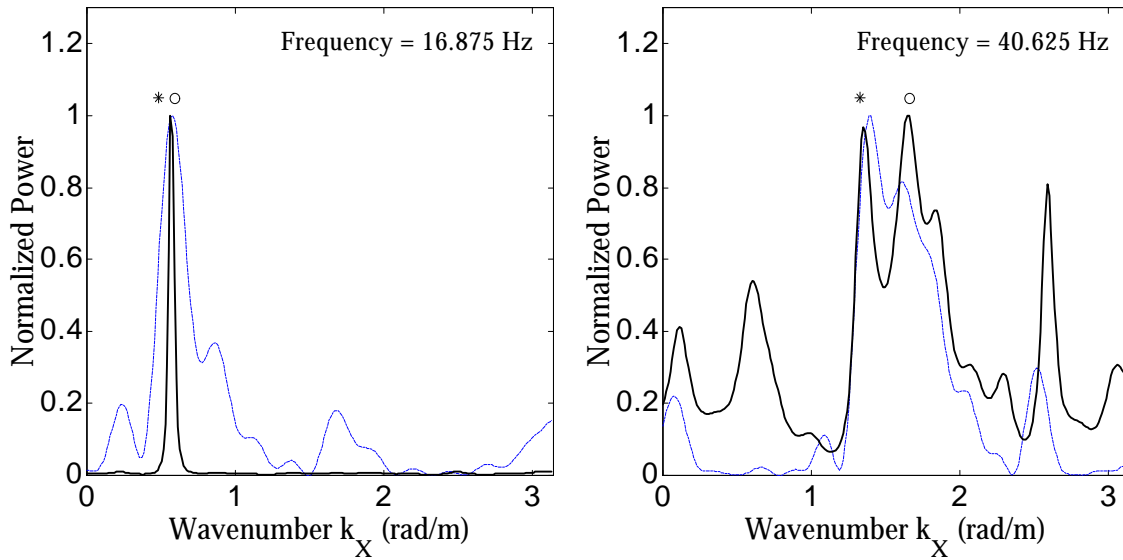


Figure 6.24 Power Spectrum Estimates for the MUSIC Method. The MUSIC estimates are shown with solid lines, and the FDBF power spectrum estimate (dashed-dot line) is shown for reference.

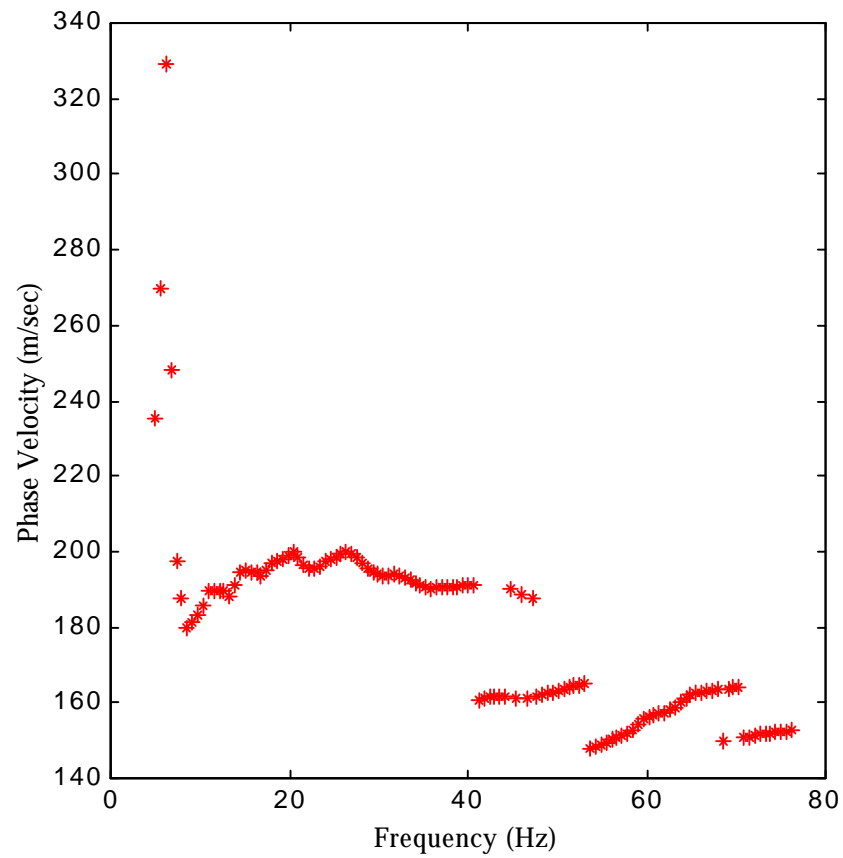


Figure 6.25 Linear Prediction Dispersion Curve Estimate. The linear prediction dispersion curve estimate, using sensor 12 as the reference, is shown with asterisks.

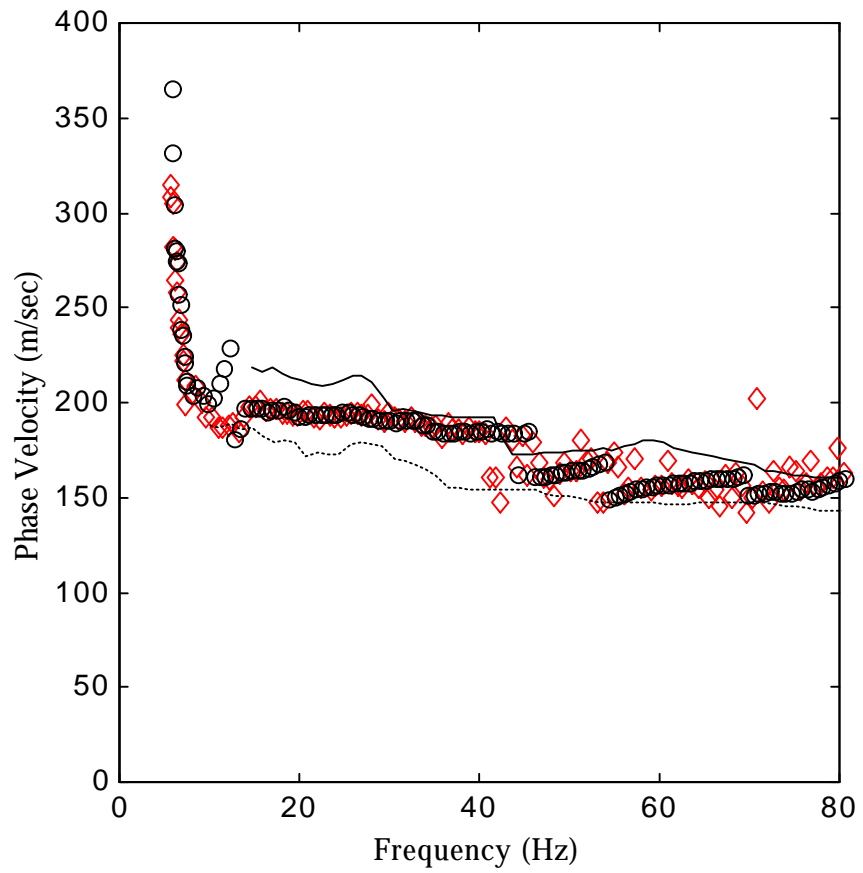


Figure 6.26 MUSIC Dispersion Curve Estimate (shown with diamonds). The FDBF estimate (circles) is shown for reference.

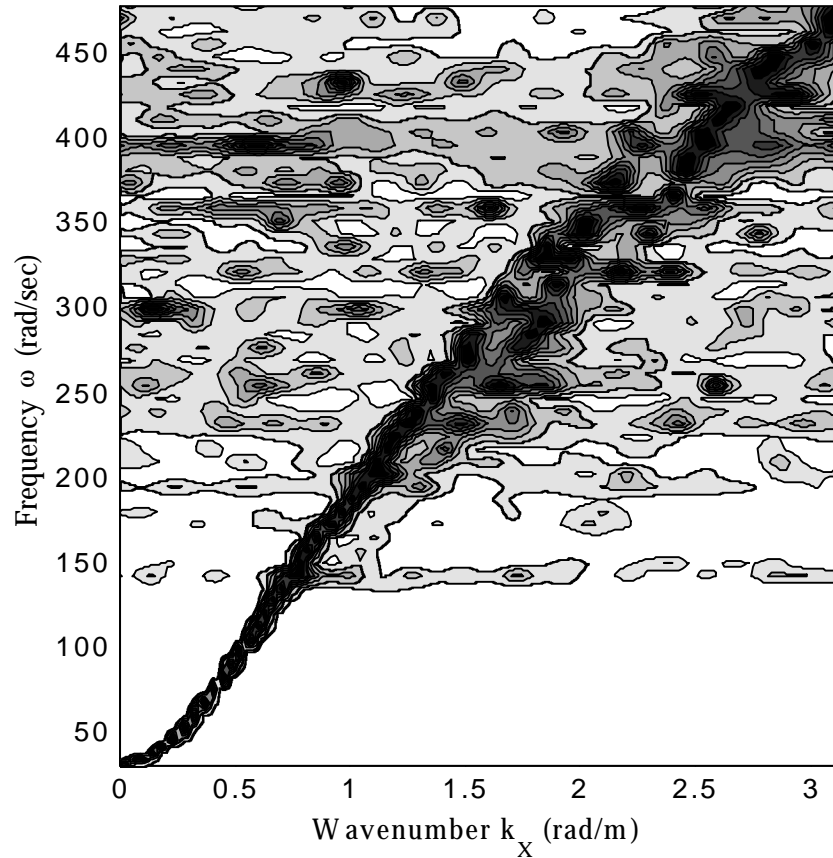


Figure 6.27 MUSIC Power Spectrum Estimate as a Function of Temporal Frequency and Wavenumber

6.10 Model Incompatibility Effects on Estimated Dispersion Curve

The model incompatibility between the actual physics of seismic wave propagation from a point source and the traditional two-point estimation methods causes the dispersion estimate to be biased. This section will discuss the model incompatibility effects and compare the traditional plane wave estimators with the correct cylindrical model. The analysis uses the most simplistic case imaginable, i.e. a single mode in a homogeneous half-space, to emphasize the limitations of the traditional two-point estimators.

6.10.1 Homogeneous Half-Space Dispersion Curve

In a homogeneous, elastic half-space, characterized by a constant shear wave velocity V_S with depth, Rayleigh surface waves are nondispersive, i.e. the phase velocity of the surface waves are constant versus frequency or wavelength. In the case of a homogeneous half-space, the Rayleigh wave phase velocity can be determined exactly as a function of the mediums' Poisson's ratio, only requiring the solution to a reduced cubic equation (Graff, 1975). The dispersion curve for a case where the half-space exhibits a constant shear wave velocity = 108.7 m/s and a Poisson's ratio $\nu = 0.25$ is shown in Figure 6.28. For this case, the Rayleigh wave phase velocity equals $0.9194 V_S$, or 100 m/s. Although the dispersion relation is simply a straight line, Figure 6.28 will be useful as a reference in the following discussion concerning the model incompatibility effects.

The dispersion relation is most commonly presented as a plot of radial temporal frequency versus wavenumber, and the curve for the homogeneous case under discussion is

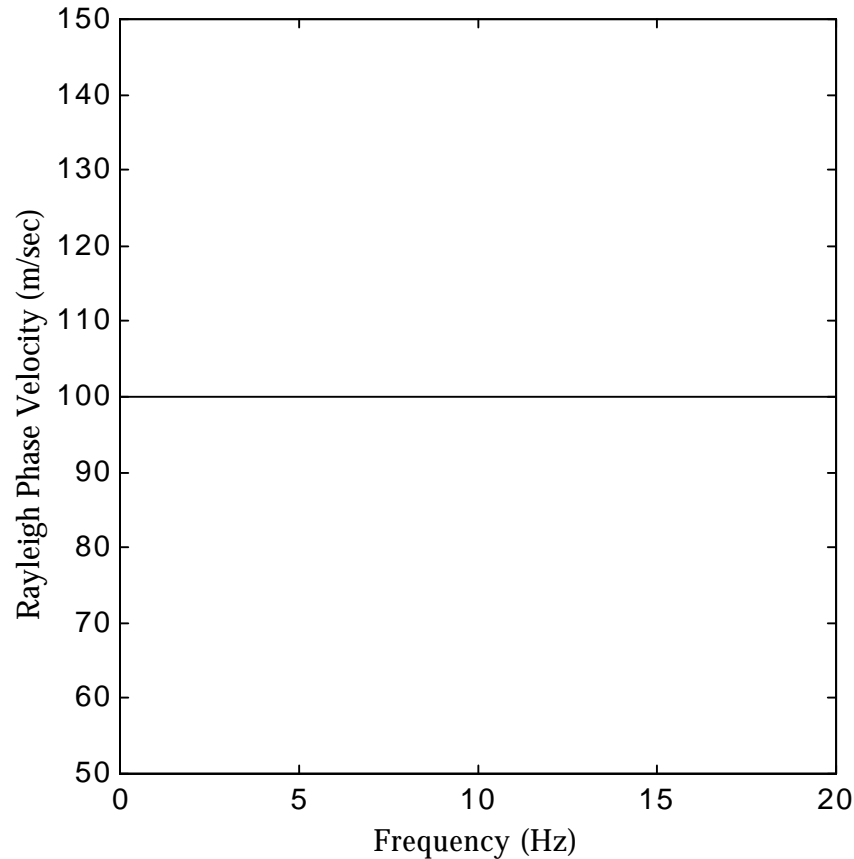


Figure 6.28 Rayleigh Wave Phase Velocity as a Function of Frequency for a Homogeneous Half-Space with $V_S = 108.76$ m/s and Poisson's Ratio $\nu = 0.25$. The phase velocity V_R equals 100 m/s for all frequencies.

shown in Figure 6.29. Figure 6.29 represents the same information as shown in Figure 6.28.

6.10.2 Dispersion Relation for Gradually Increasing V_S with Depth to Infinity

An explicit definition of phase velocity will help clarify the following discussion. Recall that in geotechnical engineering analysis of seismic surface waves, several different measures of phase velocity have been used, including apparent and effective. The latter terms only exist due to the inability of traditional estimators to sift out individual modes of propagation.

Consider a half-space where the shear wave velocity V_S equals 108.7 m/s at the surface and gradually increases with depth. The dispersion relation in this case is shown in Figure 6.30, and the homogeneous half-space example is shown for reference. Notice that the two lines asymptotically approach each other with increasing wavenumber, and

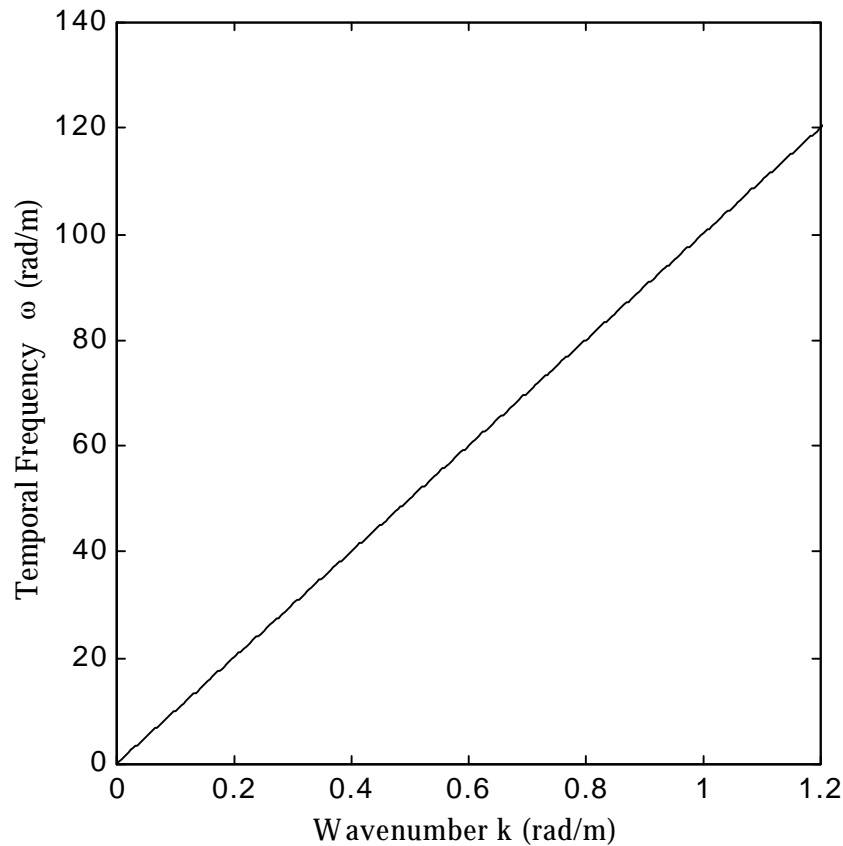


Figure 6.29 Dispersion Relation for Homogeneous Half-Space with $V_R = 100$ m/s